Anion and Cation Order in Iodide-Bearing Mg/Zn−Al Layered Double Hydroxides

Laure Aimoz,*,[†,‡] Christine Taviot-Guého,[§,‖] Sergey V. Churakov,[†] Marina Chukalina,[⊥] Rainer Dähn,[†] Enzo Curti,[†] Pierre Bordet,[#] and Marika Vespa[∇,○]

[†]Laboratory for Waste Management, Paul Scherrer Institute, 5232 Villigen PSI, Switzerland

[‡]Institute of Geological Sciences, University of Bern, Baltzerstrasse 1-3, 3012 Bern, Switzerland

[§]Clermont Université, Université Blaise Pascal, Institut de Chimie de Clermont-Ferrand, BP 10448, 63000 Clermont-Ferrand, France

[‖]Laboratoire des Matériaux Inorganiques, CNRS, UMR 6002, 63177 Aubière, France

[⊥]Institute of Microelectronics Technology RAS, 6 Institutskaya Street, 142432 Chernogolovka, Russia

[#]Institut Néel, CNRS et Université Joseph Fourier, BP 166, 38042 Grenoble, cedex 9, France

[∇]Department of Chemistry, Division of Molecular and Nanomaterials, Dutch−Belgium Beamline, European Synchrotron Radiation Facility, Catholic University of Leuven, BP 220, 38043 Grenoble, France

[○]Institute for Transuranium Elements, European Commission, BP 2340, D-76125 Karlsruhe, Germany

S *Supporting Information*

ABSTRACT: Uptake of iodine in hydrotalcite-like minerals is a potential retardation mechanism for dose-relevant [129]I in the near-field of a deep repository for radioactive waste. The location of iodide in (Zn/Mg)Al layered double hydroxides (LDH) was investigated using a combination of advanced atomic-scale techniques. Wavelet transform analysis of Zn K-edge extended X-ray absorption fine structure (EXAFS) spectra and geometry optimization based on ab initio density functional calculations allowed the distribution of Al^{3+} in the cationic layer to be determined. Using Rietveld refinement of synchrotron X-ray powder diffraction data (XRD) and EXAFS at the I K-edge enabled the average location of iodide in the interlayer to be established. Additional short- and medium-range structural information was also obtained from the pair distribution function analysis of the XRD data in support of the findings obtained with the long- and short-range techniques. By combining the results, a local order of Al^{3+} in Zn₂Al−I and Zn₃Al−I LDHs was shown generating hexagonal and orthorhombic supercells, respectively. Furthermore, an uncorrelated distribution between I⁻ anions and Zn^{2+}/Al^{3+} cations was demonstrated, resulting from a dynamic disorder of water and iodide position in the interlayer space.
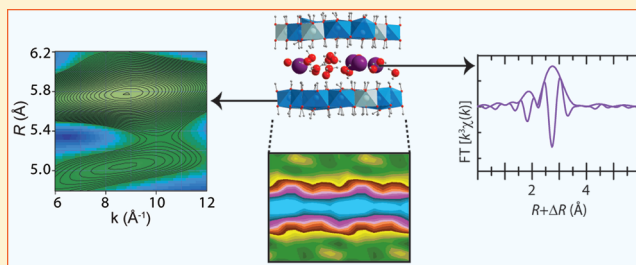
INTRODUCTION

Radioactive waste is foreseen to be disposed of in deep geological repositories within chemically durable waste matrices (borosilicate glass, cement), engineered barriers with high sorption capacities (bentonite backfill), and suitable host-rocks (clay formations). For instance, spent fuel from nuclear power plants contains significant amounts of [129]I. This iodine will eventually be released as dissolved anionic species (I⁻ or IO₃⁻) as soon as groundwater comes into contact with the degrading radioactive waste.[1] [129]I is predicted to be dose-determining in safety analyses due to its long half-life (1.57×10^7 years) and its weak retention by major minerals in the repository near-field (e.g., clays and carbonates). Up until now, the effect of minor minerals able to bind anionic species such as layered double hydroxides (LDH) has not been fully taken into account. The most common naturally occurring LDH is hydrotalcite $[Mg_{0.8−0.67}Al_{0.2−0.33}(OH)_2][(CO_3)_{0.10−0.16}(H_2O)_{2−3}]$. LDH phases may occur in the cementitious materials of the waste

matrix or in the engineered barrier or in adjacent rocks altered by pore water from cements.[2]

The structure of LDH consists of positively charged hydroxide layers and intercalated charge-compensating exchangeable anions surrounded by water molecules. Their general formula is $[M^{2+}_{1-x}M^{3+}_x(OH)_2][X^{−n}]_{x/n}\cdot yH_2O$, abbreviated hereafter as $(M^{2+})_rM^{3+}−X$, in which M^{2+} = Mg, Zn, Co, Ni, Mn, etc. and M^{3+} = Cr, Fe, V, Co, etc.; A^{n-} is an anion or an oxy−anionic complex (inorganic or organic); and $r = (1 − x)/x$ with $x \in [0,1]$ is the M^{2+}/M^{3+} molar ratio usually ranging between 2 and 4.[3] Iodide could be incorporated in LDH phases due to its anionic nature and, thus, reduce [129]I mobility. A mechanistic understanding, particularly at the atomic scale, of

the binding of I^- to LDH phases is therefore of great relevance to the performance assessments of radioactive repositories.

It is well-known that LDH properties such as anion exchange capacity are strongly influenced by the cation ordering and by the location of anions.[3,4] However, the charge distribution is still a matter of debate because most structural studies deal with powdered samples. Information on the atomic configuration of LDH provided by X-ray diffraction (XRD) is limited due to the small particle size. In addition, structural disorders cannot systematically be detected due to the insufficient difference in the scattering power of M^{2+} and M^{3+} cations and the low scattering power of the interlayer anions. For example, ordering of the cations within the hydroxide layers should occur at a $M^{2+}/M^{3+} = 2$, according to Pauling's rule on the nature of coordinated polyhedra (avoidance of $M^{3+}-M^{3+}$ as close neighbors in polyhedra).[5] However, this ordering of cations has hardly been confirmed experimentally by powder XRD, with the exception of Ca_2Al LDH, $LiAl_2$ LDH, and the sulfated form of green rusts.[6-9] However, other techniques such as extended X-ray absorption fine structure (EXAFS) spectroscopy and solid-state nuclear magnetic resonance (NMR) combined with molecular dynamic simulation can provide a better insight into the charge distribution in LDH systems. For instance, using EXAFS spectroscopy, a local order (for the first metal shell) was demonstrated for $Co^{2+}-(Fe^{3+}+Al^{3+})$ LDH,[10] $Cu^{2+}-Cr^{3+}$ LDH,[11] and also $Mg^{2+}-Fe^{3+}$LDH[12] systems with $M^{2+}/M^{3+} = 2$. Other studies relying on the wavelet analysis based on an ab initio code (named FEFF) of the EXAFS spectra at the Zn K-edge up to 6.2 Å showed an ordered positioning of $Zn(OH)_6$ and $Al(OH)_6$ octahedra in Zn_2Al-NO_3.[10-13] Further, using a combination of ^1H, ^{27}Al, and ^{25}Mg NMR, the ordering of Mg and Al was demonstrated for $Mg^{2+}/Al^{3+} = 2$.[13] However, a newer study indicated the presence of a certain amount of Al clustering with $Al-O-Al$ linkages.[14] Finally, recent calculations based on plane-wave density functional theory indicated a preferred stability of the cation-disordered Mg_rAl-Cl LDH upon increasing values of r. This was explained by the decrease in the number of $Al-O-Al$ linkage.[15] The effect of cation distribution on the arrangement of interlayer anions is not fully understood. Indeed, a few studies report anion ordering in LDH system for sulfate,[6] silicate,[16] and carbonate[17] anions. Radha et al. observed a certain degree of stacking order matching the symmetry of the interlayer sites for (Ni, Co)Al LDH intercalated with CO_3^{2-}, Cl^-, and SO_4^{2-} anions.[18] Many other studies, based on molecular dynamic simulation and aiming at a better understanding of the behavior of interlayer species, indicate that the interaction energies of small inorganic anions such as CO_3^{2-}, Cl^-, and SO_4^{2-} with the LDH host structure are stronger than the interaction with larger organic anions.[15,19-27] Recently, Prasanna et al. investigated the interlayer structure of (Mg/Zn)$_r$Al LDH intercalated with halide anions (Cl^-, Br^-, I^-) using powder XRD data.[28,29] These authors found some indications of positional disorder of I in the interlayer based on the extinction of characteristic reflections of the MgAl-I LDH XRD pattern and obtained a best fit to a simulated pattern by assuming a combination of positional disorder and turbostraticity.

Relatively little attention has been paid to the structure of the interlayer space, and further studies are required to gain a thorough understanding of the relationship between the distribution of cations and anions in the layer and interlayer, respectively. A major objective of the present study was to investigate whether an ordered cation distribution in the hydroxide layer of (Mg/Zn)$_r$Al-I LDHs could induce a local order of the iodide anions in the interlayer because this may have consequences on the thermodynamic stability of the compound and, therefore, also on the potential retardation of ^{129}I during the alteration of cementitious radioactive waste. A series of (Mg/Zn)Al-(I,IO$_3$) LDH with different M^{2+}/M^{3+} ratios were synthesized and the structures were characterized using advanced experimental and theoretical techniques to resolve both short- and long-range structural order. FEFF-based wavelet transforms of Zn K-edge EXAFS spectra combined with atomistic calculations based on density functional theory (DFT) allowed the local order of metal ions in the hydroxide sheet to be determined. Atomistic ab initio calculations were also performed to support the results from the wavelet analysis by determining the energetically most favorable distribution of Zn and Al in the hydroxide layer at a Zn/Al ratio of 3. In addition, I K-edge EXAFS spectra were measured for the first time to probe the coordinative environment of iodide in the interlayer space of LDH. So far, only a few EXAFS studies at the I K-edge have been reported, either for physical studies[30-35] or to solve more complex structures.[36,37] Finally, in the case of Zn_4Al-I, high-resolution synchrotron X-ray diffraction data allowed us to determine the averaged structure from Rietveld refinement and to calculate the pair distribution function (PDF). The PDF has only been applied recently to LDH systems[38] and was successfully used in this study to determine the deviation of the short-range atomic arrangement from the average crystal structure and also to get medium-range structural information.

■ METHODS

Synthesis of (Mg/Zn)Al-I LDH. All chemicals were at least of pro analysis grade. Solutions were prepared using deionized and decarbonated water. Each LDH phase ($[M^{2+}_{1-x}M^{3+}_x(OH)_2][X^{-n}]_{x/n}\cdot yH_2O$) was synthesized by coprecipitation at constant pH (Table 1) following established procedures.[39]

Table 1. Synthesis Conditions for (Mg/Zn)Al LDH Phases ($[M^{2+}_{1-x}M^{3+}_x(OH)_2][X^{-n}]_{x/n}\cdot yH_2O$) Prepared by Coprecipitation at Constant pH

	M^{2+}	M^{3+}	M^{2+}/M^{3+}	X^{m-}	pH	temp (°C)
Mg$_2$Al-I	Mg^{2+}	Al^{3+}	2	I$^-$	9.2	23 ± 2
Zn$_2$Al-I	Zn^{2+}	Al^{3+}	2	I$^-$	6.4	60 ± 2
Zn$_3$Al-I	Zn^{2+}	Al^{3+}	3	I$^-$	9.5	23 ± 2
Zn$_4$Al-I	Zn^{2+}	Al^{3+}	4	I$^-$	8.8	23 ± 2
Zn$_2$Al-IO$_3$	Zn^{2+}	Al^{3+}	2	IO$_3^-$	8.4	60 ± 2
Zn$_2$Al-NO$_3$	Zn^{2+}	Al^{3+}	2	NO$_3^-$	9.2	23 ± 2

Syntheses were carried out under an N_2 gas flow to avoid carbonate contamination. One molar solutions of M^{2+} and M^{3+} nitrate salts ($M^{2+} = Mg^{2+}$ or Zn^{2+} and $M^{3+} = Al^{3+}$) were slowly added ($\sim$0.1 mL/min) into a magnetically stirred iodide, iodate, or nitrate solution (KI, KIO$_3$, or KNO$_3$). The anion carrier solution was stoichiometrically 5 times in excess to favor the formation of the iodide-bearing phase. The pH was maintained constant by a slow addition of a freshly prepared 2 M NaOH solution using an automated titrator. The suspension was further aged for 24 h and centrifuged and the supernatant discarded. Finally, the solid was washed twice with deionized water. Iodide-containing ZnAl LDH solids were synthesized at

various ratios of Zn^{2+}/Al^{3+} (2, 3, and 4). Synthesis pathways were optimized by varying pH and temperature in order to obtain the most crystalline samples (Table 1).

Chemical Analysis of the Solids. A fraction of each solid was digested with 1% Suprapur HNO_3 to assess Zn, Mg, and Al content using an Applied Research Laboratory ARL 3419D inductively coupled plasma optical emission spectrometer (ICP-OES).

To assess the iodide and nitrate contents, I^- and NO_3^- were displaced from the interlayer with CO_3^{2-}. For this purpose, 100 mg of each solid were placed in a 0.1 M K_2CO_3 solution. I^-, IO_3^-, and NO_3^- were quantitatively exchanged due to the large excess of CO_3^{2-} (~10 times) and the large stability of CO_3-containing LDH phases. After 48 h on an end-over-end shaker, the solid samples were filtered through 0.2 μm nylon filters and measured by high performance ion-exchange chromatography using a Dionex DX-600 ion chromatograph with an IonPac AS16/AG16 column.

Thermogravimetry (TG) measurements were performed in order to determine the contents of interlayer water using a Mettler Toledo TGA instrument. The weight loss was measured between 60 and 1000 °C with a heating rate of 5 °C/min, after 8 h of preheating at 60 °C to remove physisorbed water. Most commonly, the determination of the water content in LDH phases is deduced from the total mass loss. However, due to the incomplete evaporation of HI from the solid, as already observed for other halide-containing LDH,[29,40,41] total mass loss cannot be applied to assess the water content. The amount of structural water was therefore estimated by assuming that structural water loss is complete at the first inflection point of the thermogravimetric curve at about 220 °C.

Powder X-ray Diffraction (XRD). Mineralogical determination of synthesized products was initially made by XRD on a PANalytical X'Pert Pro diffractometer equipped with a X'Celerator detector and a Cu anticathode ($K\alpha_1/K\alpha_2$). The instrument was used in the $\theta-\theta$ reflection mode, fitted with a nickel filter, 0.04 rad Soller slits, 10 mm mask, 1/2° fixed divergence slit, and 1/4° fixed antiscatter slit. XRD data were measured over a range of 5−70° (2θ) with a step size of 0.0167° and a total counting time of about 3 h. Considering the $R\bar{3}m$ space group typical for LDH, the cell parameters were determined from peak profile analysis (full pattern matching) with the FullProf suite programs[42,43] using the TCH (Thompson−Cox−Hasting) pseudo-Voigt function.[44] Backgrounds were refined by adjusting the height of preselected points for linear interpolation. The relatively high crystallinity of Zn_4Al−I allowed us to attempt a Rietveld structure refinement using high-resolution powder X-ray diffraction data collected on the CRISTAL beamline at the synchrotron Soleil. A monochromatic beam of wavelength 0.4388 Å tuned with a double crystal Si(111) monochromator was used. Each sample was loaded in a rotating 0.7 mm diameter glass capillary, which was mounted on a two-circle diffractometer equipped with 21 multianalyzer crystals. The Rietveld refinement was carried out with the FullProf suite programs using the TCH pseudo-Voigt function to fit the experimental profiles.[42−44] Structural refinements were performed considering the $R\bar{3}m$ space group and taking as initial values those reported for Zn_2Al−Cl.[19] The instrumental contribution to peak broadening was determined with a $Na_2Ca_3Al_2F_{14}$ (NAC) standard. The resulting instrumental resolution function ($U = 2.29 \times 10^{-4}$, $V = 2.1 \times 10^{-5}$, $W = 4 \times 10^{-6}$, $X = 1 \times 10^{-6}$, $Y = 5.44 \times 10^{-4}$) was included in the refinement. The XRD pattern is characterized by anisotropic shape broadening attributed to the small crystallite size and the presence of microstrains. To treat anisotropic size effects, the Lorentzian part of the peak broadening was modeled with linear combinations of spherical harmonics, which allowed the calculation of the crystallite average size along each reciprocal lattice vector.[45] Assuming disk-shaped crystallites, the apparent size for the 00l reflections corresponds to the thickness of the disk, and the diameter is obtained from the apparent size for hk0 reflections multiplied by $3\pi/8$.[46] An "average apparent shape" of the crystallite can also be displayed using the GFOURIER program of the FullProf suite. Anisotropic strain effects were also considered using a model based on the Stephens formalism.[47] GFOURIER program was also used for calculating electronic density maps.

The same set of diffraction data was used for the pair distribution function (PDF) analysis. The PDF method is based on the total scattering pattern, where the Bragg peaks and the diffuse component both reflect the average longer-range atomic structure and the local structural imperfections.[48] At first, the diffraction pattern was corrected for background, which was determined using a separate diffraction measurement of an empty glass capillary and taking into account Compton scattering, absorption, and polarization. All these corrections were done using the program PDFgetX2.[49] Subsequently, the corrected X-ray diffraction data were scaled into electron units and the structure function $S(Q)$ was calculated. The PDF, which gives the probability to find an atom at a distance r away from another atom, was obtained by a Fourier transformation of $S(Q)$ according to eq 1.

$$G(r) = \frac{2}{\pi} \int_0^\infty Q[S(Q) - 1] \sin Q(r) \, dQ \tag{1}$$

where Q is the magnitude of the scattering vector. $S(Q)$ was truncated at $Q_{max} = 25.4$ Å^{-1}, the signal-to-noise ratio being unfavorable beyond that value of Q. To investigate the structure of Zn_4Al−I, the simulated PDFs based on the Rietveld structure were compared to the experimental PDF using the software PDFFIT.[50]

In order to check for potential phase transition as reported for Cl- and Br-containing CaAl LDH,[51] a low temperature XRD measurement of Zn_4Al−I sample was carried out at the powder diffraction station of the SNBL beamline (BM01B) of the European Synchrotron Radiation Facility (ESRF, Grenoble, France).[52] The sample was mounted in a 0.7 mm capillary and cooled down by a liquid nitrogen flux at 100 K. The photon beam wavelength was calibrated using the NIST silicon standard (640C) and a Rietveld refinement of the data, yielding $\lambda = 0.5020$ Å. The X-ray diffraction pattern of Zn_4Al−I at 100 K was found to be identical to the room-temperature pattern, indicating the absence of phase transition (see Supporting Information SI.1).

Ab Initio Structure Optimization. For a theoretical interpretation of EXAFS data, the structures of the iodide-containing samples (Mg_2Al−I, Zn_2Al−I, Zn_3Al−I, and Zn_4Al−I LDHs) were obtained by geometry optimization based on density functional theory (DFT)[53] using the Gaussian and plane waves method as implemented in the CP2K simulation package.[54] Core electrons were taken into account using dual space norm-conserving pseudopotentials.[55] Valence electron orbitals were expanded using the DZVP-MOLOPT-SR atom-centered Gaussian basis set.[56] The electron charge density was expanded using an auxiliary plane wave basis set up to a 320 Ry cutoff. The PBE (Perdew−Burke−Ernzerhof) exchange and

correlation functionals[57] used in the calculations were shown to reproduce best the lattice parameters of LDH phases.[15] A set of test calculations has also been performed using PBE functionals augmented with a dispersion correction (DFT+D)[58] for the Zn_3Al-I system. A similar setup was successfully applied for modeling the solvation of I^- and IO_3^-.[31,59] Except for the H_2O molecules and I atoms in the interlayer, the initial atomic configuration for the optimization runs was taken from XRD data. H_2O molecules and I atoms were initially placed in the middle of the interlayer, below M^{2+} and M^{3+} sites, respectively. The position of hydrogen atoms in OH and H_2O groups is unknown, and thus, the protons were assigned to corresponding oxygen sites at a 1 Å distance. The modeled supercells contained $(6 \times 6 \times 1)$, $(4 \times 4 \times 1)$, and $(5 \times 5 \times 1)$ crystallographic unit cells in optimization runs of $(Mg/Zn)_2Al-I$, Zn_3Al-I, and Zn_4Al-I LDHs, respectively. The lattice parameters were fixed throughout the geometry optimization to the one provided by the analysis of XRD data (Table 3). Al sites were distributed in octahedral layer according to the Pauling's rules. At a $M^{2+}/Al^{3+} = 2$, Al was initially positioned in a honeycomb configuration (Figure 1a), by introducing

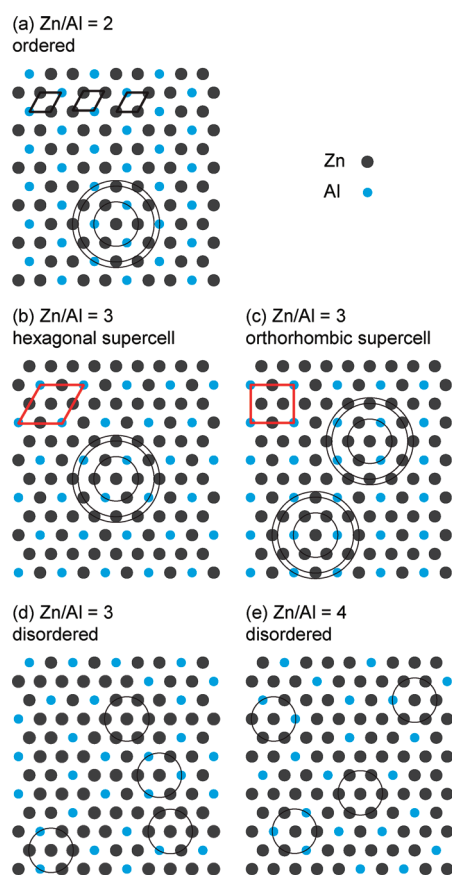**Figure 1.** Possible arrangements of M^{2+} and M^{3+} cations in LDH sheets according to Pauling's rule, which requires every M^{3+} to be surrounded by M^{2+} as nearest neighbors. (a) Zn/Al = 2, honeycomb arrangement as the only possible configuration. Zn/Al = 3 with various possible arrangements: (b) with a hexagonal supercell, (c) with an orthorhombic supercell, and (d) in a disordered configuration. (e) Zn/Al = 4, an example of a disordered configuration. Circles represent the subsequent coordination shells of M^{2+}/M^{3+} octahedral around M^{2+} cation. The supercells are represented as red quadrilaterals. The potential subcells to be considered with a side length of a (i.e., unit cell parameter) are represented as black parallelograms in part a.

stacking faults over the three sheets in the cell. Structure and relative energies of Zn/Al = 3 LDHs with hexagonal, orthorhombic, and disordered arrangement of Al sites (Figure 1, parts b, c, and d, respectively) in $(8 \times 8 \times 1)$ supercells were obtained using both DFT and DFT+D methods.[58] These simulations were employed to investigate the stability of different cationic arrangements in LDHs and test the importance of dispersion correction for the system of interest. At Zn/Al = 4, Al was placed in a disordered pattern (for example, Figure 1e). Various disordered configurations for Zn/Al = 3 and 4 were investigated. In all cases, a random stacking of adjacent hydroxide layers was introduced. In the initial configurations, iodide and water molecules were located in the middle of the interlayer plane, above Al and (Zn, Mg) atoms, respectively.

Zinc and Iodine K-Edge EXAFS Analysis. Zinc and iodine K-edge bulk EXAFS spectra were collected at the Dutch−Belgium Beamline (BM26A) of the ESRF.[60] Measurements were collected using a He cryostat set to 90 K for all samples. Measurements at lower temperature did not improve the data quality (see Supporting Information SI.2).

For the Zn K-edge, the Si(111) monochromator angle was calibrated by assigning an energy of 9659 eV to the first inflection point of the corresponding edge measured with a Zn metal foil. Samples and references were measured in transmission mode with ionization chambers filled with 90%−10% He−Ar mixture (I_0) and an 80%−20% Ar−He mixture (I_t), respectively. Radial structure functions (RSF) were obtained by Fourier transformation of the k^3-weighted $\chi(k)$ function between 3.2 and 16.4 $Å^{-1}$ with a Kaiser−Bessel window and a smoothing parameter of 1.0.

For the I K-edge, the Si(111) monochromator angle was calibrated by assigning the energy of 33169 eV to the first inflection point of the corresponding edge measured with a KI reference compound. Samples and references were measured in transmission mode with ionization chambers filled with 100% Ar (I_0) and a 50%−50% Kr−Ar mixture (I_t). Radial structure functions (RSF) were obtained by Fourier transformation of the k^3-weighted $\chi(k)$ function with a Kaiser−Bessel window and a smoothing parameter of 1.0. A narrow k range from 2.3 to 8.3 $Å^{-1}$ was selected in order to eliminate the high level of noise observed at high k. All EXAFS data reduction was performed using the IFEFFIT software package (Athena and Artemis) following standard procedures.[61,62] After background subtraction and normalizing the spectra by fitting a first- and a third-degree polynomial, respectively, the energy was converted to photoelectron wave vector units ($Å^{-1}$) by assigning the threshold energy, E^0, to the first inflection point of the absorption edge.

EXAFS data analysis was performed by a multishell fitting of inverse Fourier transform (FT^{-1}). The R-range selected for the FT^{-1} was from 1.5 to 6.2 Å at the Zn K-edge and from 2.2 to 3.5 Å at the I K-edge. The amplitude reduction factor (S_0^2) was set to 0.85[63,64] for the Zn spectra and to 1.0 for the I spectra after fitting the KI reference and according to previously published data.[31] Theoretical scattering paths for the fit were calculated using FEFF8.4 (ab initio calculations to model the EXAFS function).[65,66] The scattering potential was calculated self-consistently using atomic configurations directly derived from ab initio geometry optimization runs. Indeed, optimized structures are assumed to provide a more reliable short-range 3D to the model based on raw crystallographic data alone and

are, thus, selected to model the experimental data (see details in Supporting Information SI.3).

In addition, FEFF-based wavelet transform analysis (WT) of the EXAFS spectra at the Zn K-edge was used to complement the Fourier transform analysis. This method was used for investigating the possible presence of Al in the various shells of the iodide-containing ZnAl LDH samples, which were initially fitted with Zn−Zn backscattering pairs alone. The Morlet wavelet, a complex sine wave localized with a Gaussian envelope, allows separating the contributions of light and heavy backscattering atoms (discriminated in k) at similar distances (similar R). However, when two shells are only partially resolved in R, the Morlet function alone is not sufficient and a FEFF-based model is required. A detailed description of the method to obtain the FEFF-Morlet has been explained elsewhere.[67] Briefly, the construction of the FEFF-Morlet wavelet is based on FEFF8.4 calculation of selected paths of interest in order to complement the Morlet wavelet with the accurate characteristics of the theoretical EXAFS function. A given path is present at a given distance when the FEFF-Morlet wavelet coincides with the signal. This coincidence can be assessed by calculating the power density function, i.e., integration over a given R range for a given path as function of the scale parameter s. The selected path is present at the given distance, if there is a maximum at $s = 1.00 \pm 0.01$, corresponding to a confidence interval of 0.998.

■ RESULTS

Chemical Analysis of the Solids. Chemical analysis was performed on each solid sample to determine their stoichiometries. Each sample was found to bear an M^{2+}/M^{3+} ratio close to the starting one in solution (Table 2). The

Table 2. Stoichiometries of LDH Phases Determined by Chemical Analysis

	M^{2+}/Al^{3+}	X^-/Al^{3+} (X = I, IO_3, or NO_3)	H_2O/Al^{3+}
Mg_2Al-I	2.0 ± 0.2	0.6 ± 0.2	2.0 ± 0.5
Zn_2Al-I	2.0 ± 0.2	0.7 ± 0.2	2.2 ± 0.5
Zn_3Al-I	3.0 ± 0.2	0.7 ± 0.2	2.8 ± 0.5
Zn_4Al-I	3.8 ± 0.2	0.8 ± 0.2	3.7 ± 0.5
Zn_2Al-IO_3	2.0 ± 0.2	0.8 ± 0.2	1.4 ± 0.5
Zn_2Al-NO_3	2.0 ± 0.2	1.0 ± 0.2	1.6 ± 0.5

anionic content is, in some cases, lower than the stoichiometry expected for pure LDH phases (e.g., one monovalent anion per Al^{3+}). This finding is attributed to a possible contamination by carbonate anions.

The amount of structural water was determined by TG and assumed to correspond to the first mass loss, after elimination of physisorbed water using a pretreatment at 60 °C. However, the probable presence of physisorbed CO_2 and the partial removal of HI expected in this temperature range may result in additional weight losses. This results in non-negligible uncertainties by attributing the first mass loss to solely water and by excluding the possible partial evaporation of structural water during the following mass loss.

X-ray Diffraction. The powder XRD patterns of hydrotalcite-like (Mg/Zn)Al LDH (Figure 2) were indexed in a hexagonal unit cell with the space group $R\bar{3}m$ by considering a random site distribution of the cations within the hydroxide layers. The cell parameters were determined from a whole-pattern fitting procedure. The interlayer distances, d_{003}, which
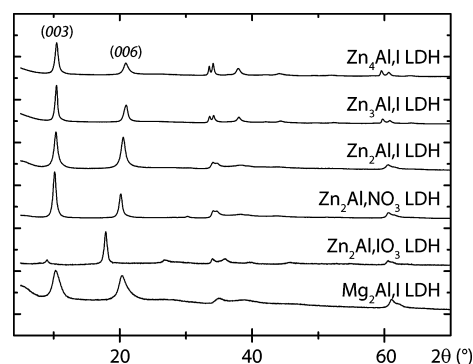

Figure 2. XRD patterns of the iodide-containing hydrotalcite-like LDH obtained using Cu Kα radiation. Intensities are plotted in arbitrary unit.

are directly related to the position of the first diffraction peak at low 2θ angles, are all consistent with the values expected for the intercalation of iodide, iodate, and nitrate in the interlayer space (Figure 3, Table 3). Although Zn_xAl-I samples appear to be
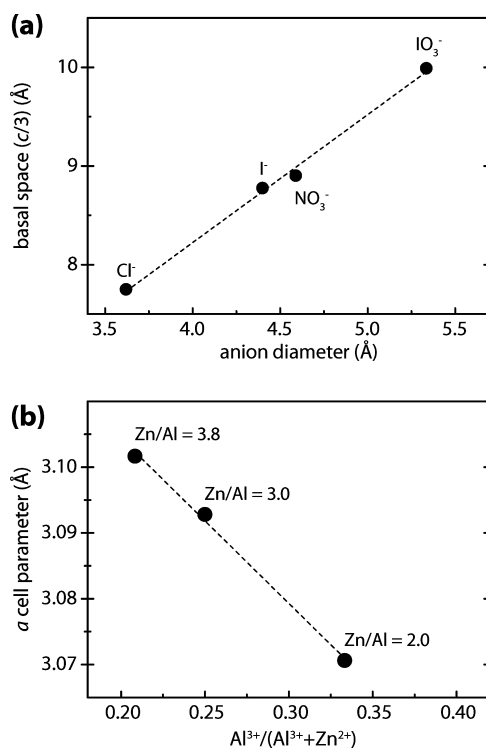

Figure 3. (a) Expansion of basal spacing in Zn_2Al LDH phase as a function of anion size in the interlayer. Chloride data was taken from Pisson et al.[19] (b) Cell parameter a vs Al^{3+} content of iodide-containing ZnAl LDH follows Vegard's law.

substantially more crystalline than Mg_2Al-I (Figure 2), the X-ray diffraction peaks are rather broad for all cases due to small particle size and lattice defects.

The interlayer distance obtained for Zn_2Al series linearly increases with increasing the size of the anions, assuming that the symmetry axis of NO_3^- and IO_3^- is perpendicular to the metal hydroxide layer and considering the ionic radii given by Shannon[68] (Figure 3a). Furthermore, the variation of the cell parameter a as a function of $x = Al^{3+}/(Zn^{2+} + Al^{3+})$ for Zn_xAl-I series is in full agreement with the values reported elsewhere for

Table 3. Results of Cell Parameters Determination (Whole-Pattern Fitting) and Rietveld Structure Refinement for Zn_4Al-I ($R\bar{3}m$)^a

		sample	a (Å)	c (Å)
full pattern matching		Mg_2Al-I	3.0532(5)	26.705(9)
		Zn_2Al-IO_3	3.0733(4)	29.964(5)
(λ Cu $K\alpha_1/K\alpha_2$ = 1.5418 Å)		Zn_2Al-NO_3	3.0293(5)	26.103(4)
		Zn_2Al-I	3.0706(5)	26.324(2)
		Zn_3Al-I	3.0928(1)	25.199(1)
		Zn_4Al-I^b	3.10164(5)	25.178(2)

Rietveld	atom	site	x	y	z	B_{iso} (Å^2)	occupancy
R_{wp} (%) =7.6/18.1	Zn	3a	0	0	0	0.64(3)	0.0667
	Al	3a	0	0	0	0.64(3)	0.0167
R_{Bragg} /R_F (%) = 6.4/5.5	O_{OH}	6c	0	0	0.3778(2)	0.64(3)	0.1667
χ^2 = 1.4	I	6c	0	0	0.16667	8.00	0.0167
	O_w	18h	0.079(9)	−0.079(9)	0.5	8.00	0.0366(8)

^{a}Standard deviations in parentheses. ^{b}Chemical formula deduced from the Rietveld refinement: $Zn_4Al(OH)_{10}I\cdot2.2H_2O$.

carbonate-containing $(Mg/Zn)_rAl$ LDH (Figure 3b) and indicates a solid solution-type behavior.

By the introduction of a strong scatterer like iodine (as I^- or IO_3^-), one can expect an XRD pattern to be more sensitive to the structure of the interlayer. Indeed, because the interlayer atoms diffract out of phase with the metal hydroxide layers, a gradual decrease of the intensity of the 003 reflection relative to the 006 can be observed (Figure 2). The intensity inversion is clear for Zn_2Al-IO_3. For Zn_rAl-I series, a gradual increase of the intensity of the 006 refection is observed as the value of R decreases; i.e., the amount of I^- in the interlayer space increases.

Rietveld Structure Refinement and Pair Distribution Function of Zn_4Al-I LDH. Owing to the relatively high crystallinity of Zn_4Al-I LDH, a Rietveld refinement of the structure using high-resolution synchrotron X-ray powder diffraction was attempted. The refinement was performed in the space group $R\bar{3}m$ considering a random distribution of the cations within the hydroxide layer. After introducing the atoms from the hydroxide layer, the positions of the interlayer species were detected thanks to a Fourier difference map calculation (Figure 4). Although the electron density spread over the whole interlayer space indicating a strong disorder, two large maxima can be distinguished on the section summed from z/c = 0.125 to 0.210 and correspond to the 6c (0, 0, z) and 18h (x, $-x$, z) Wyckoff positions. The height of the peak at (x, $-x$, z) is about 4/5 of the height of the peak at (0, 0, z), which allows one to attribute the 6c and 18h positions to iodide and water molecules (O_w), respectively.

The final refined values of cell parameters, atomic positions, and atomic displacement parameters are reported in Table 3 and a graphical representation of the refinement is given in Figure 5. The implementation of corrections for anisotropic broadening and anisotropic microstrains was essential to reach acceptable reliability factors. Selected distances are tabulated for comparison with the results from geometry optimization and from EXAFS (Tables 4 and 5). The site occupancy of O_w refined to a value of 7.3% led to the chemical formula $Zn_4Al(OH)_{10}I(H_2O)_{2.2}$. Except from H_2O content, the stoichiometry is in relatively good agreement with the chemical analysis, giving $Zn_{3.8\pm0.2}Al(OH)_{10}I_{0.8\pm0.2}(H_2O)_{3.8\pm0.5}$. Note that the number of water molecules determined by Rietveld refinement corresponds to structural water molecules belonging to the crystalline phase. Results from TG resulted in higher water content, but these measurements are representative of
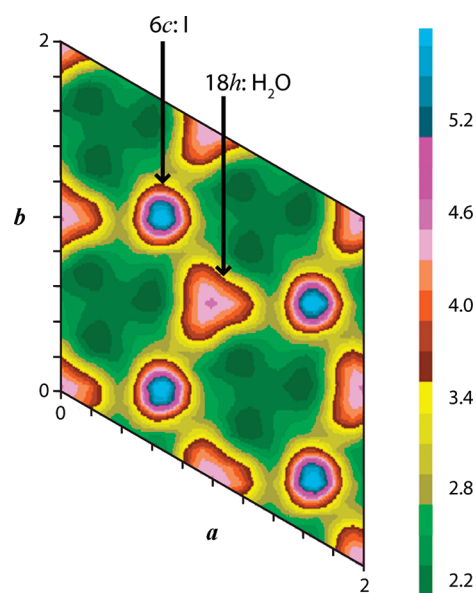

Figure 4. Contoured electronic Fourier difference map in the (a,b) plane (summed for one interlayer space from 0.125 to 0.210 along the c axis) obtained after introducing atoms from the hydroxide layer. Two main density spots are observed corresponding to 6c and 18h Wyckoff positions and are attributed to I and H_2O, respectively. The electronic density scale is given on the right in arbitrary unit (au).

the bulk sample (both amorphous and crystalline components) and may overestimate the actual water content in the crystalline LDH phase. The 6c position for iodine atoms is aligned with Zn and Al cations along the c direction and equidistant from the hydroxyl groups of the adjacent layers (Table 4). This position corresponds to a prismatic interlayer site. Strong correlations were observed between the atomic coordinates and the atomic displacement parameters (ADP). To reduce these correlations, interlayer species (I, O_w) and atoms of the hydroxide layers (Zn, Al, O_{OH}) were constrained to have identical ADP values. The ADP parameters for the interlayer species were fixed to a value of 8.0 Å^2 in accordance with the results reported elsewhere[69] and were consistent with the existence of interlayer disorder. In addition, the average distance Zn/Al−O_{OH} was refined separately and fixed during the refinement of the other parameters. If not constrained, an overly large value of M−O_{OH} bond length is obtained. This instability of the refinement is assumed to be due to the

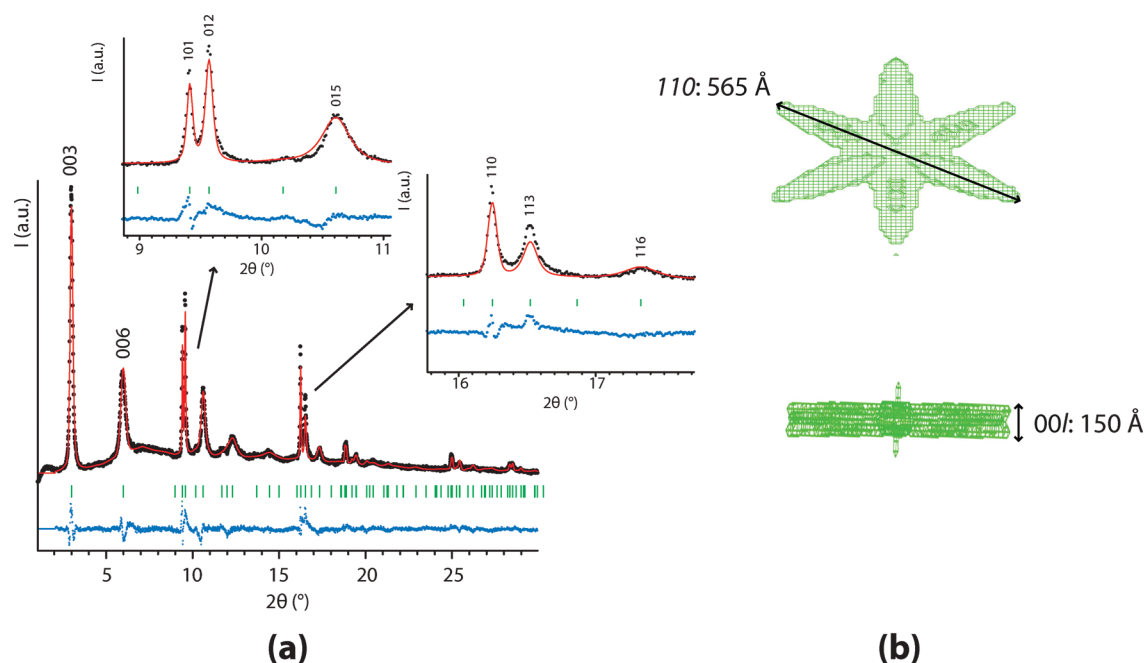**Figure 5.** (a) Rietveld refinement results for Zn_4Al-I LDH measured at room temperature: Experimental powder X-ray diffraction pattern (black dots), calculated pattern (solid red line), Bragg reflections (green ticks), and difference profiles (blue dots, at the bottom). (b) Average apparent shape and size of the crystallite coherence domain in the specified directions.

relatively low crystallinity of the powder and the presence of a strong disorder.

Furthermore, although the present structure model appears to be sound, it should be admitted that the implementation of such correction for anisotropic broadening using spherical harmonics can lead to a misinterpretation of the scattering from such disordered systems. Therefore, our structure model requires further conclusive experimental evidence. When comparing our diffraction pattern with the DIFFaX-simulated patterns of the model structures,[28] one can notice the strong intensity of the 015 reflection, which agrees well with the location of the halide ion in the 6c site (Figure 5). Positioning I^- in 6c position (instead of e.g. 18h) leads to an $I-O_{OH}$ distance of 3.560(4) Å, which is in good agreement with the one obtained by EXAFS and geometry optimization (see below and Table 5). In addition, the location of I^- in the vicinity of the metal cations of the hydroxide layers is consistent with the large size of I^-, promoting Coulombic interactions and, thus, compensating the poor H-bonding ability of this anion.

As already mentioned, the anisotropic peak broadening has been modeled as a linear combination of spherical harmonics. Besides, in order to account for some structural disorder, the contribution of microstrain to peak broadening was also evaluated. The coherent domains reconstructed from the refined spherical harmonic coefficients are in total agreement with the hexagonal platelet shape of LDH crystals (Figure 5b). From the values determined in the directions normal to the 110 and 00l reflecting planes, the average apparent diameter L_{110} of 565 Å and thickness L_{00l} of 150 Å of the platelets can be determined. From this latter value one can also calculate an approximate number of stacking layers per crystallite to be ∼18. On the other hand, the Zn_4Al-I XRD pattern appears to be strongly affected by microstrains (ε) in the stacking direction with a value of $\varepsilon_{00l} = 233 \times 10^{-4}$ compared to $\varepsilon_{110} = 17 \times 10^{-4}$ along the in-plane direction of the platelets. Microstrains in the LDH system can be caused by different kinds of structural

disorder such as (i) intergrowth of different polytypes, (ii) turbostratic disorder, and (iii) interstratifications. For the Zn_4Al-I material of this study, the observed nonuniform broadening of the h0l/0kl is indicative of a random intergrowth of $2H_1-3R_1$ polytypes.[3] In contrast, turbostratic disorder seems to be absent because besides a broadening of the 0kl reflections, the 113 reflection should additionally be affected, which is not observed here. Finally, the broadening of the 006 reflection (fwhm 0.34° 2θ) with respect to the 003 reflection (fwhm 0.18° 2θ) and the pronounced sharpness of the 012 reflection (fwhm 0.07° 2θ) strongly suggest interstratification phenomena that may arise from the cointercalation of some nitrate anions during the synthesis (introduced by the nitrate salts). This could also explain the high level of microstrains determined along the c stacking direction.

While Rietveld refinement gives an average view of the structure of the material, the PDF analysis can be used to get medium-range structural information. Indeed, the PDF is representative of both the average longer-range atomic structure and the local structural imperfections. Using the same set of diffraction data as for Rietveld refinement, the PDF of Zn_4Al-I LDH was investigated. The oscillations of the PDF extend over 50 Å in accordance with the crystalline character of the material (Figure 6a).

However, the effect of atomic displacive disorder is obvious due to the appearance of split and broad peaks. The first peak, corresponding to the closest O_{OH} shell around Zn/Al atoms, displays a left shoulder and can be modeled by the superposition of two components (Figure 6b). By fitting this peak with two Gaussians two distances are found at 1.86 and 2.08 Å, which can be unambiguously attributed to $Al-O_{OH}$ and $Zn-O_{OH}$ bonds, respectively. The $Zn-O_{OH}$ distance is in excellent agreement with the results from EXAFS (see section on EXAFS spectroscopy at the Zn K-edge). To our knowledge, this is the first time that an atomic pair distribution function could resolve $Al-O_{OH}$ and $Zn-O_{OH}$ bonds in an LDH

Table 4. Structural information Derived from the Zn K-Edge EXAFS Analysis of ZnAl LDH Samples Compared to the Results of Rietveld Refinement and Geometry Optimization of the Structure (G Opt.), when available[a]

	bond	method	CN	R (Å)	σ^2 (Å²)	R-factor	ΔE^0 (eV)
Zn_2Al–I	$Zn-O_{OH}$	EXAFS	6[b]	**2.10(1)**	0.005	0.10	−2.8 ± 2.0
		G Opt.	6	2.11(3)			
	Zn–Al	EXAFS	3[c]	3.03(3)	0.007		
		G Opt.	3	**3.07(3)**			
	Zn–Zn	EXAFS	3[c]	**3.09(1)**	0.005[e]		
		G Opt.	3	3.07(3)			
	Zn–Zn	EXAFS	6[c]	**5.35(1)**			
		G Opt.	6	5.32(4)			
	Zn–Zn	EXAFS	3[c]	6.01(2)			
		G Opt.	3	**6.14(4)**			
Zn_2Al-NO_3	$Zn-O_{OH}$	EXAFS	6[b]	2.09(1)	0.005	0.10	−4.1 ± 1.9
	Zn–Al	EXAFS	3[c]	3.05(3)	0.008		
	Zn–Zn	EXAFS	3[c]	3.08(1)	0.005[e]		
	Zn–Zn	EXAFS	6[c]	5.33(1)			
	Zn–Zn	EXAFS	3[c]	5.98(2)			
Zn_2Al-IO_3	$Zn-O_{OH}$	EXAFS	6[b]	2.10(1)	0.006	0.10	−3.5 ± 1.8
	Zn–Al	EXAFS	3[c]	3.05(3)	0.006		
	Zn–Zn	EXAFS	3[c]	3.08(2)	0.005[e]		
	Zn–Zn	EXAFS	6[c]	5.33(1)			
	Zn–Zn	EXAFS	3[c]	5.99(2)			
Zn_3Al–I	$Zn-O_{OH}$	EXAFS	6[b]	**2.10(2)**	0.007	0.08	−0.8 ± 1.7
		G Opt.	6	2.11(6)			
	Zn–Al	EXAFS	3.2 ± 0.6[d]	3.02(3)	0.007		
		G Opt.	2.0[f]	**3.09(3)**			
	Zn–Zn	EXAFS	2.8 ± 0.6[d]	**3.11(1)**	0.004[e]		
		G Opt.	4.0[f]	3.10(3)			
	Zn–Zn	EXAFS	2.9 (±0.7)	**5.39(1)**			
		G Opt.	4.7[f]	5.36(4)			
	Zn–Zn	EXAFS	5.9 ± 0.6	6.06(1)			
		G Opt.	4.7[f]	**6.19(4)**			
Zn_4Al–I	$Zn-O_{OH}$	EXAFS	6[b]	**2.11(2)**	0.007	0.08	0.5 ± 1.7
		Rietveld	6	2.112(3)			
		G Opt.	6	2.12(10)			
	Zn–Zn/Al	Rietveld	6	3.10			
	Zn–Al	EXAFS	3.2 ± 0.6[d]	3.02(3)	0.004[e]		
		G Opt.	1.5[f]	**3.11(3)**			
	Zn–Zn	EXAFS	2.8 ± 0.6[d]	**3.11(1)**			
		G Opt.	4.5[f]	3.12(6)			
	Zn–Zn	EXAFS	3.1 ± 0.8	**5.39(1)**			
		G Opt.	5.1[f]	5.38(5)			
	Zn–Zn	EXAFS	6.3 ± 0.7	6.06(1)			
		G Opt.	4.7[f]	**6.21(5)**			

[a]CN, R, σ^2, R-factor, and ΔE^0 are coordination number, interatomic distance, Debye−Waller factor, goodness of the fit as defined in IFEFFIT,[62] and shift of the threshold energy, respectively. S_0^2 was fixed to 0.85. When different techniques are applied, values for distances based on the most reliable technique are in bold. [b]Fixed to 6 for the first hydroxide shell. [c]Fixed according to Pauling rules for Zn/Al = 2. [d]Sum of coordination number of Zn and Al was fixed to 6.0. [e]Debye−Waller factors of Zn−Zn backscattering pairs were constrained to be identical for all shells in each sample. [f]CN fixed by the initial structure selected for the geometry optimization with an orthorhombic substitution of Al atoms at a Zn/Al = 3 and with a random substitution of Al atoms at a Zn/Al = 4.

structure. This finer analysis is attributed to the high resolution provided by the use of high-energy synchrotron X-ray diffraction measurements.

The experimental PDF was also compared to the PDF calculated from the Rietveld averaged structure for $r \leq d_{003}$. Only a partial match in peak positions and intensities could be obtained (Figure 6c). Thus, the more local information obtained with the PDF slightly deviates from the long-range distance Rietveld average structure. These local deviations first concern the M−O$_{OH}$ pairs for the average structure model which is constrained to have a single M−O$_{OH}$ bond length. The

Rietveld structure also fails in reproducing the PDF peak widths, probably because the atomic displacement parameters do not model positional disorder correctly. In contrast, the peaks attributed to the M−M bond distances observed at a (~3.09 Å), $\sqrt{3}a$ (~5.38 Å), and $2a$ (~6.20 Å) are well fitted, indicating reliable site occupancies. Removing the interlayer content has almost no effect on the calculated PDF, indicating the minor contribution of interlayer species to the total diffracted intensity (Supporting Information SI.4). The comparison over a wider r range, i.e., beyond the interlayer distance, reveals more important misfits due to the micro-

Table 5. Structural Information Derived from the EXAFS Analysis of the (Mg/Zn)Al LDH Samples Measured at the I K-Edge; Estimation of the Coordination Number and Average Distance from Geometry Optimization Are Tabulated for Comparison[a]

	bond = I−O	CN	R (Å)	σ^2 (Å^2)	ΔE^0 (eV)	R-factor
Mg$_2$Al−I LDH	geometry optimization	**9.4**	**3.58(22)**			
	EXAFS fit	8.7 ± 2.4	**3.59(3)**	0.019	0.9 ± 1.3	0.01
Zn$_2$Al−I LDH	geometry optimization	**9.6**	**3.61(20)**			
	EXAFS fit	10.0 ± 2.7	**3.58(3)**	0.021	−1.5 ± 1.4	0.01
Zn$_3$Al−I LDH	geometry optimization	**10.9**	**3.50(19)**			
	EXAFS fit	8.6 ± 2.2	**3.55(3)**	0.019	−4.6 ± 1.6	0.01
Zn$_4$Al−I LDH	Rietveld refinement I−O$_{OH}$ only[b]	6.0	3.560(4)			
	geometry optimization	**10.7**	**3.57(18)**			
	EXAFS fit	8.8 ± 4.1	**3.57(5)**	0.019	−1.5 ± 2.4	0.04

[a]CN, R, σ^2, R-factor, and ΔE^0 are coordination number, interatomic distance, Debye−Waller factor, goodness of the fit as defined in IFFEFFIT,[62] and shift of the threshold energy, respectively. S_0^2 was fixed to 1.0. Accepted values for distances and coordination numbers based on the most reliable technique are in bold. The reported uncertainties in the EXAFS and Rietveld results arise from the fit and refinement calculations, whereas the reported uncertainties in the geometry optimization results correspond to the standard deviation of the estimated average distance. [b]Due to the high multiplicity and low occupancy of the O$_w$ sites, I−O$_w$ unique distances cannot be extracted from Rietveld refinement; therefore, only I−O$_{OH}$ distances are presented here.
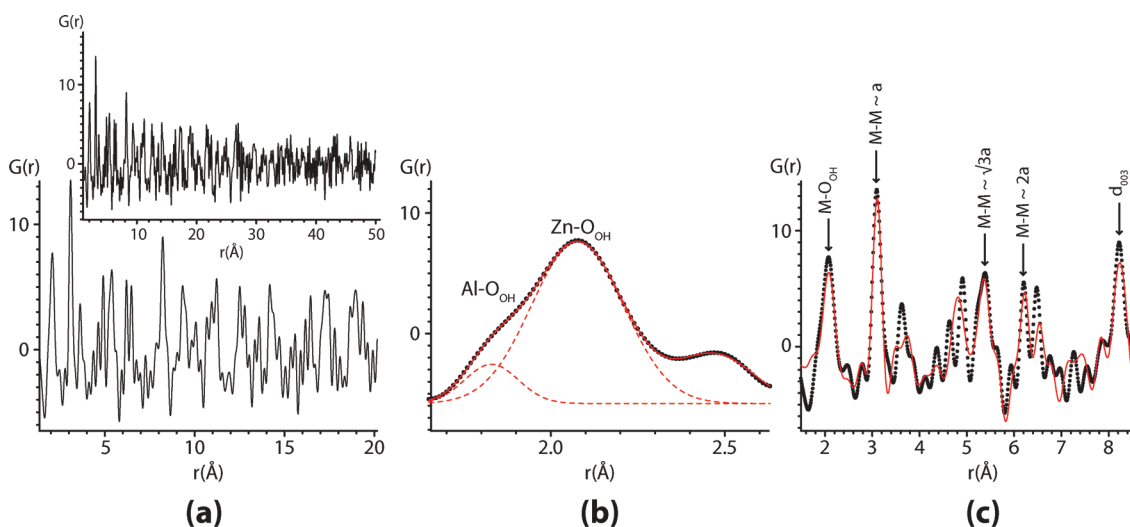

Figure 6. (a) Experimental pair distribution function of Zn$_4$Al−I. (b) Gaussian fit to the first peaks in the PDF: experimental data (black dots), fitted data (plain red line), individual Gaussians (dotted red line); peaks are labeled with the corresponding atomic pairs. (c) Experimental PDF compared to the PDF calculated from the Rietveld averaged structure up to r = d$_{003}$: experimental data (black dots), fitted data (plain red line); arrows indicate expected interatomic distances.
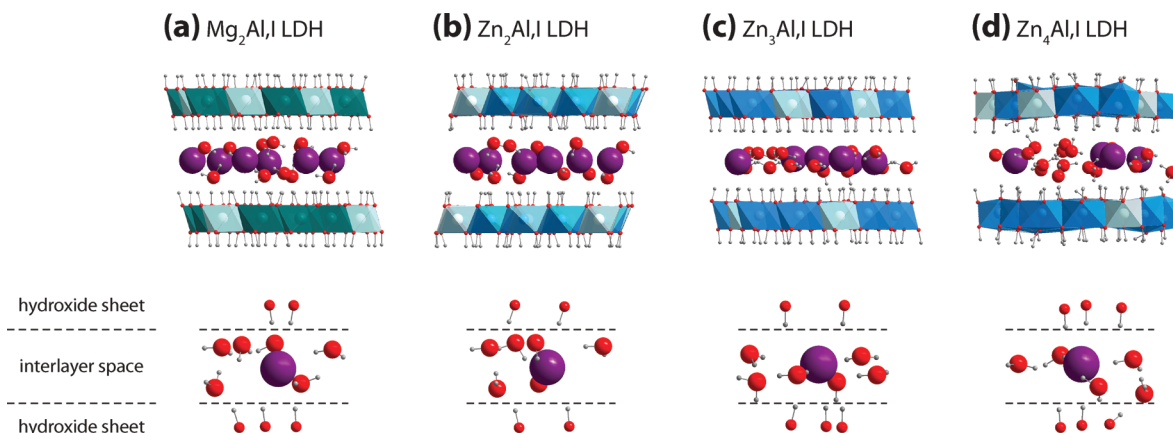

Figure 7. Coordination environment of I atom (in a sphere of ∼4 Å) as obtained by geometry optimization based on ab initio simulations for (Mg/Zn)Al−I LDH phases. I atoms are represented by violet spheres. Oxygen atoms from water molecules in the interlayer are large red spheres bonded with two protons (gray). Oxygen atoms from OH groups [small red spheres bonded with protons (gray)] form corners of Mg/Zn (green/blue) and Al (light blue) polyhedra. The octahedral sheet is slightly corrugated at high Zn/Al ratio (in c and especially d). Note that oxygen atoms in the selected sphere originate not only from water molecules but also from hydroxide groups.

Table 6. Relative Lattice Energies of $Zn_3Al(OH)_8I\cdot3H_2O$ Structures for Different Distribution of Al Cations, Given as Differences to the Energy Obtained for an Orthorhombic Distribution of Al Atoms[a]

	$\Delta E(4\times4\times1,DFT)$ (kJ·mol^{-1})	$\Delta E(8\times8\times1,DFT)$ (kJ·mol^{-1})	$\Delta E(8\times8\times8,DFT+D)$ (kJ·mol^{-1})	$-T\Delta S^{conf}$ (kJ·mol^{-1})
orthorhombic	0	0	0	0
disordered	NA	51.7	48.1	−11.2
hexagonal	108.7	106.1	125.0	0

[a]NA = not available.
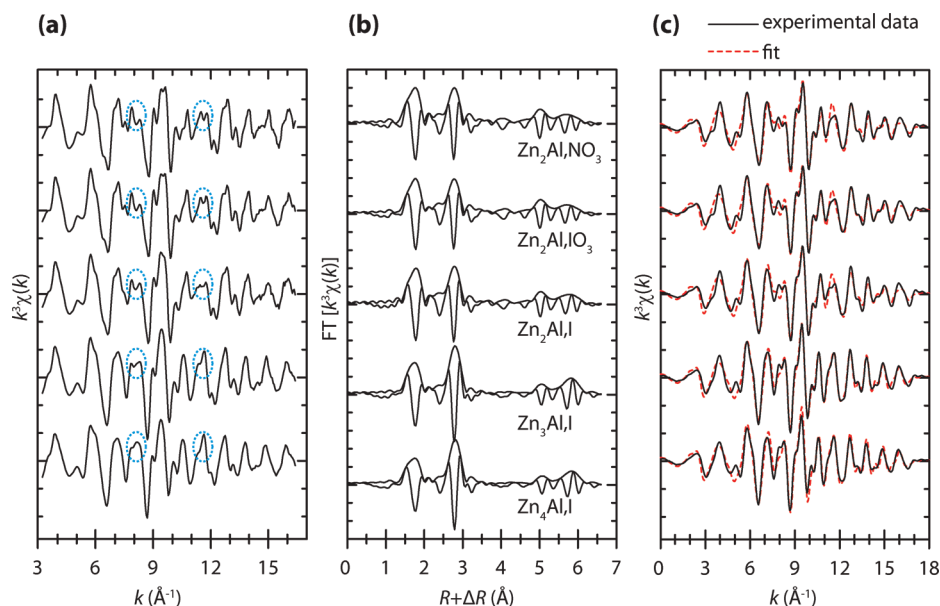
Figure 8. Experimental Zn K-edge EXAFS spectra and corresponding fit models of the various ZnAl LDHs, measured at 90 K: (a) k^3-weighted, (b) FT, and (c) FT^{-1}. Typical features (i.e., beat patterns) associated with the Zn/Al ratio are circled in part a (blue dashed circles).

structural disorders identified above, polytype intergrowth, and interstratifications phenomena. Owing to the difficulty in handling both structural disorder and microstructural component, no refinement of the PDF data was attempted here.

Geometry Optimization. The geometries of iodide-containing LDH structures were obtained by lattice energy minimization and were used as input for the theoretical interpretation of measured EXAFS data. The average interlayer distance ($=c/3$) calculated from the Zn and Al positions remained the same after geometry optimization within 0.1%. The mean square displacement of Mg/Zn and Al atoms with respect to the ideal crystallographic positions in the c direction was small at $M^{2+}/Al^{3+} = 2$ (~0.02 Å) but was larger at higher Zn/Al ratios (0.07 and 0.20 Å at $Zn^{2+}/Al^{3+} = 3$ and 4, respectively), indicating a stronger disorder at higher ratios (Figure 7d). However, Zn−Zn and Zn−O distances obtained from Rietveld refinement agree, within uncertainties, with the results of geometry optimization in the Zn$_4$Al−I LDH structure.

The I−O radial distribution function (RDF) (including both O$_w$ and O$_{OH}$) is given in the Supporting Information (SI.5). A schematic of the oxygen atoms from O$_w$ and O$_{OH}$ surrounding iodine at short-range distance is illustrated in Figure 7. The I−O RDF of the investigated structures has a single maximum at 3.4−3.5 Å and a slowly decaying tail. The coordination numbers and average I−O distances were calculated by integrating the radial distribution function up to 4.0 Å. The structural parameters derived from geometry optimization are summarized in Table 5.

The lattice energies of the optimized Zn$_3$Al−I LDH structures (with different arrangements of Al substitution) were calculated relative to the optimized structure with the orthorhombic distribution of Al atoms (Table 6). The results obtained for the small supercell (4 × 4 × 1) are in good agreement with the larger one (8 × 8 × 1), indicating a good convergence of the lattice energy with respect to k-points. The contribution of dispersion correction to the relative energy and geometry of the studied structures was found to be negligible by comparing the results obtained by PBE and by PBE+D. The simulations show that the structure with orthorhombic arrangement of Al substitutions has a lower lattice energy compared to hexagonal and disordered arrangements. To compare the relative stability of the structures, the contribution of configurational entropy for the disordered structure has to be taken into account. For the same structures with identical composition, the other terms can be neglected to a first approximation. The maximum contribution due to this term can be estimated by assuming ideal mixing between Al/Zn sites and I−H$_2$O sites (eq 2)

$$-T\Delta S^{conf} = nRT[(x_{A1} \ln x_{A1} + x_{Zn} \ln x_{Zn}) + (y_I \ln y_I + y_{H_2O} \ln y_{H_2O})] \qquad (2)$$

where x_i and y_j are mole fractions of corresponding components, R is the gas constant, T is the temperature, and n is the number of formula units. For the disordered phase with the composition $Zn_3Al(OH)_8I\cdot3H_2O$, n is equal to 4, and the configurational entropy contribution is −11.2 kJ·mol^{-1}. This value is significantly smaller than the difference in the internal
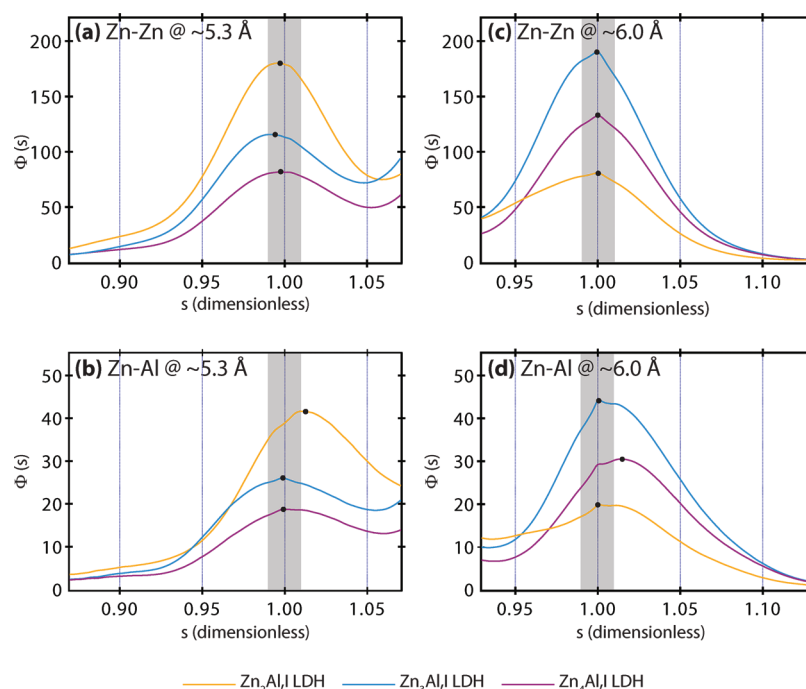
Figure 9. Power density functions obtained using FEFF-Morlet wavelets for Zn/Al ratios equal to 2, 3, and 4: (a) second metal shell with Zn−Zn backscattering pair at ~5.3 Å. (b) second metal shell with Zn−Al backscattering pair at ~5.3 Å, (c) third metal shell with Zn−Zn backscattering pair at ~6.0 Å, and (d) third metal shell with Zn−Al backscattering pair at ~6.0 Å. Black dots are plotted to help visualize the maxima. The gray stripe represents $s = 1.00 \pm 0.01$.

lattice energy between the disordered structure and the one with orthorhombic distribution of Al substitutions. The structure with the hexagonal distribution of cations has significantly larger lattice energy (i.e., energetically unfavorable), which is in good agreement with results from the wavelet analysis ruling out a hexagonally ordered structure (See FEFF-based WT of the EXAFS spectra the Zn K-edge).

EXAFS Spectroscopy at the Zn K-Edge. EXAFS spectroscopy at the Zn K-edge was used to determine the distribution of atoms in the octahedral sheet and to verify if the presence of a heavy backscattering atom like iodine in the interlayer would be detectable in the EXAFS spectra. This could indicate a locally ordered distribution of iodine atoms with respect to Zn. All k^3-weighted EXAFS spectra are similar, in spite of varying Zn/Al ratios and different interlayer anions (Figure 8). In particular, all k^3-weighted spectra show a distinctive beat pattern at 7 Å^{-1} < k < 9 Å^{-1} (Figure 8a, circled in blue), which is caused by the destructive interference of Zn and Al. This feature is typical for LDH phases.[70−73] Note that this beat pattern is more pronounced for samples with higher Al content (i.e., lower Zn/Al ratios). Furthermore, a splitting of the EXAFS oscillations is observed at 11.5 Å^{-1} (Figure 8a, circled in blue), which is also associated with the Al content. These results indicate that the EXAFS spectra are sensitive to changes in the Zn/Al ratio, indicating different structural environments around Zn atoms. This results in different amplitudes of some of the peaks in the FT, although the distances are similar for all samples. Four main shells are observed in the FT between ~2 and ~6 Å. The first peak at $R + \Delta R = 1.7$ Å corresponds to the Zn−O backscattering pair in octahedral coordination.[72] At larger distances, three Zn−Zn and/or Zn−Al backscattering pairs were identified ($R + \Delta R$ = 2.8, 5.0, and 5.8 Å).[67] The FT peaks at $R + \Delta R$ = 2.8 and 5.8 Å show a higher amplitude for the Zn$_3$Al and Zn$_4$Al samples,

whereas the FT peak at $R + \Delta R = 5.0$ Å shows the highest amplitude for the Zn$_2$Al sample. Thus, the amplitude of the FT peak correlates with the Zn/Al ratio. This indicates that the FT peaks at $R + \Delta R$ = 2.8, 5.0, and 5.8 Å are mostly associated with the presence of Zn−Zn backscattering pairs.

All spectra for the different Zn/Al ratio and anionic species could be well-fitted with Zn−O at $R \sim 2.1$ Å and Zn−Zn/Al backscattering pairs at R = ~3.1, 5.3, and 6.0 Å (Table 4). The Zn−O, Zn−Zn, and Zn−Zn pairs at ~2.1, ~3.1, ~5.3 Å, respectively, are in good agreement with results obtained from geometry optimization, when available.

In contrast, the Zn−Al backscattering pair was difficult to fit due to the superposition of the Zn−Zn and Zn−Al backscattering pairs, especially at low Al content, and this was in most cases neglected. For instance, one expects from crystal symmetry considerations to find a Zn−Zn pair at ~6 Å at exactly twice the distance of the first metallic shell, i.e., at ~6.2 Å. This expectation is, however, not confirmed by EXAFS fitting, which systematically yields shorter distances (i.e., < 6.0 Å). This inconsistency may be explained by considering that the results from the EXAFS fit, obtained using only Zn−Zn single scattering paths to model the metallic shell at ~6 Å, may be biased by the presence of Zn−Al paths and of multiple scattering paths at similar distances.

The fact that the spectra of the iodide-containing LDH samples do not significantly differ from the spectra of LDH intercalated with NO_3^- (a light backscatterer, not detectable at large distances) is a clear indication that there is no preferential coordination between Zn and I.

FEFF-Based WT of the EXAFS Spectra the Zn K-Edge. In order to detect if Al backscatterer atoms are present in the fitted Zn shells, WT was performed. The Morlet WT alone was not sufficient to adequately resolve both k- and R-space (see Supporting Information, SI.6) due to an overlapping of the
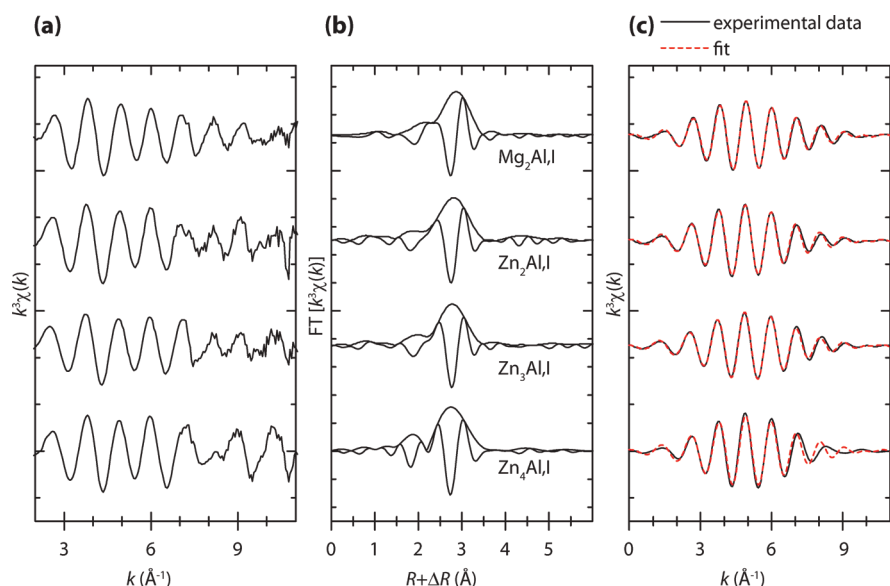
Figure 10. Experimental EXAFS spectra and corresponding fit models at the I K-edge of the (Mg/Zn)Al–I LDH, measured at 90 K: (a) k^3-weighted, (b) FT, (c) FT^{-1}.

shells at $R + \Delta R = \sim 5.0$ and 5.8 Å (Figure 8b). Therefore, the FEFF-Morlet function was used to increase the resolution in R-space. FEFF-based paths were determined using the results from the EXAFS fits in order to calculate the real FEFF-Morlet wavelets.[67] From this real FEFF-Morlet wavelet, the corresponding power density functions were computed (Figure 9). As previously mentioned, a selected backscattering pair is present at the given distance if there is a maximum at $s = 1.00 \pm 0.01$.

The power density function for the Zn–Zn backscattering pairs always presents a maximum at $s = 1.00 \pm 0.01$ (see Figure 9a,c), confirming that Zn is present in both second and third metal shells in all samples, at $R \sim 5.3$ and 6.0 Å, respectively. For the second metal shell (at $R \sim 5.3$ Å), the power density function of the Zn–Al backscattering pair displays a maximum at $s = 1.00$ for Zn/Al = 3 and Zn/Al = 4, whereas the maximum is displaced toward higher s values for Zn/Al = 2 (Figure 9b). These results imply that Al is present in the second shell at a Zn/Al ratio of 3 and 4 but not at a Zn/Al ratio of 2. Thus, for Zn₂Al–I LDH, the second shell is entirely occupied by Zn atoms, confirming the honeycomb distribution of Al at a Zn/Al of 2. For the third metal shell (at $R \sim 6.0$ Å), the power density function of the Zn–Al backscattering pairs displays a maximum at $s = 1.00$ for Zn/Al = 2 and 3 indicating the presence of Al. This implies that a hexagonal distribution of Al in the hydroxide sheet can be excluded. In contrast, for Zn/Al = 4, the absolute maximum is displaced toward higher s in the shell at $R \sim 6.0$ Å, indicating that Al is absent at $R \sim 6.0$ Å. Nonetheless, at Zn/Al = 4, a small deviation from the curve resulting in a local maximum at $s = 1.00$ is observed, which may imply some heterogeneities, i.e. the presence of minor isolated domains with Al at $R \sim 6.0$ Å.

EXAFS Spectroscopy at the I K-Edge. In order to better resolve the local distribution and coordinative environment of iodide in the interlayer of (Mg/Zn)Al LDH phases, EXAFS spectroscopy was performed at the I K-edge. The k^3-weighted EXAFS spectra are very similar for all samples and show sinusoidal oscillations, with an envelope maximized in the lower k-range (2–8.3 Å^{-1}) (Figure 10). This observation would

indicate that a relatively light (low Z) backscattering atom contribution (low k) prevails for all samples.

The corresponding FTs show a single shell at $R + \Delta R \sim 2.8$ Å (Figure 10b). The single shell was successfully fitted in all samples assuming only oxygen neighbors from interlayer water molecules and hydroxide groups (Table 5). The Debye–Waller factors (σ) were found for every sample to be fairly large (~ 0.020 Å^2), which is in good agreement with the large scatter in the distribution of the I–O distances derived from geometry optimization. This large value points to a high degree of local disorder of the iodide and oxygen atoms. In addition, the absence of further shells in the FTs indicates that the coordination between iodide atoms and cations is not detectable and, therefore, is expected to be weak. These results agree with the Zn K-EXAFS analysis showing that there is no short-range preferential coordination between metal ions (Zn) from the hydroxide sheet and iodide from the interlayer.

■ DISCUSSION

The multimethod technique developed in this study allowed for a detailed atomic description of the cation distribution in the hydroxide layer and anions in the interlayer space for a wide range of (Mg/Zn)ₓAl–I composition. Iodide can be incorporated in hydrotalcite-like (Mg/Zn)Al minerals via coprecipitation at constant pH and under an N₂ flux. An expansion of the basal spacing correlates to the size of the intercalated anions in the series NO₃⁻, I⁻, and IO₃⁻ for Zn₂Al LDH (Figure 3a). This result is consistent with previous work asserting that the basal spacing is fixed by the size of the anion as long as its size exceeds the one for water molecules and as long as the interlayer is filled with single layers of anions.[74] Our findings are also consistent with those obtained for Ca₂Al LDH with an interlayer filled with the halide series varying from Cl⁻ to I⁻.[51] In addition, we examined the effect of the charge density in the hydroxide layer and demonstrated that iodide anions are capable of balancing the cationic charge of ZnₓAl LDH layers over an M^{2+}/M^{3+} ratio between 2 and 4.

An ordered distribution of the cations, if it does exist, is not easily demonstrated experimentally. Hofmeister et al.[75]

simulated XRD patterns for a variety of LDHs in both ordered and disordered forms. They found that the calculated intensity of superlattice reflections arising from an ordered stacking of layers was always of a much weaker intensity than the one arising from the hexagonal subcell of disordered layers. They concluded that superlattice reflections are probably impossible to detect owing to the low crystallinity of LDHs. As a consequence, the XRD patterns of the present materials were all indexed using a hexagonal subcell of dimension a, in which the distribution of the cations is completely disordered. In addition, the cell parameter a was found to decrease linearly with increasing Al site mole fraction (Figure 3b). Because Al^{3+} is smaller than Zn^{2+}, this finding is consistent with the formation of a solid solution.

For the Zn_4Al-I LDH sample a Rietveld refinement of the structure was attempted using high-resolution synchrotron powder X-ray diffraction data. A preferential location of iodine on 6c position, i.e., close to the metal cations of the hydroxide layers, was refined. This location is consistent with a reinforced Coulombic interaction between iodide and cations, which would be in agreement with the poor H-bonding ability of the large iodide anions. On the other hand, the large value of the atomic displacement parameters for the interlayer species (8.0 $Å^2$) and the high level of strain detected along the c-stacking direction ($\varepsilon_{00l} = 233 \times 10^{-4}$) are indicative of a strong disorder in the interlayer space. A wide distribution of interatomic distances (large peaks) is shown by the PDF analysis, which emphasizes the atomic disorder in this iodide-containing LDH with a technique probing medium-range distances.

The short-range distance environments around Zn cations in the hydroxide layers and around I anions in the interlayer space were investigated by means of Zn and I K-edge EXAFS spectroscopy, respectively. Furthermore, thanks to the FEFF-based WT analysis of the Zn K-edge spectra, it was possible to discriminate between Al and Zn contributions for each fitted shell within the hydroxide layer. Indeed, for the Zn_2Al-I sample, the wavelet analysis of the Zn K-edge EXAFS spectrum clearly indicates the absence of Al neighbors in the second metal shell at $\sqrt{3}a \sim 5.3$ Å, which is in good agreement with Pauling's rule. A similar result was reported previously for a nitrate-containing Zn_2Al LDH.[67] This finding, although at short-range distance, actually implies a unique possible distribution of Al^{3+} in the hydroxide layer. This results in a long-range honeycomb distribution of Al atoms defining the hexagonal supercell (Figure 1a). Similarly, the wavelet analysis of the Zn K-edge EXAFS spectrum for the Zn_3Al-I sample showed that Al cations are present both in the second (~ 5.3 Å) and third ($2a \sim 6.0$ Å) metal shells. This is also in favor of an ordered arrangement of the Al^{3+} cations, with an orthorhombic supercell (Figure 1c). This result is supported by lattice energy calculations, in which the orthorhombic structure was demonstrated to be energetically the most favorable one. Finally, for the Zn_4Al-I sample, one cannot discriminate between an ordered and disordered cation distribution, but it is assumed to be mostly disordered due to the low site fraction of Al^{3+} cations. This argument justifies the choice of a subcell without regular distribution of Zn and Al for the Rietveld refinement (i.e., any of the subcell represented in Figure 1a being possible).

There is a general consensus that the distribution of the positive charge in LDH hydroxide layers is determined by the distribution of trivalent cations, i.e., Al^{3+}. Therefore, a locally ordered distribution of the cations in Zn_2Al-I and Zn_3Al-I

samples should, in principle, induce a local order of the iodide anions within the interlayer space, which should have some effect on the thermodynamic stability (solubility) of the compound. However, our results point to a local disorder of the iodide anions in all samples (Zn_2Al-I, Zn_3Al-I, and Zn_4Al-I LDHs) without any relationship to the cation distribution. The I K-edge EXAFS spectra obtained for all samples were similar, indicating a comparable coordination environment around iodide anions in all samples, with only one oxygen shell fitted with 9–10 oxygen atoms originating from both structural water and hydroxides. Besides, the I–O backscattering pair displays a large Debye–Waller factor indicating a strong local disorder. A similar value was found for iodide in pure water, therefore implying a water-like environment for iodide in the interlayer space of (Mg/Zn)Al LDHs. Because of such a disorder, no preferential coordination between iodide and the metal ions can be detected by EXAFS at both Zn and I K-edge. In conclusion, our results indicate that the ordering of cations does not affect the position of iodide ions and that, therefore, the interlayer iodide is rather loosely bound to the positively charged hydroxide layer. This is significant, as it implies that though the cations are ordered, the interlayer species behave as if the cationic layer was charge homogeneous.

■ CONCLUSION

The investigation of the location of charged centers in (Mg/Zn)$_r$Al–I LDH using advanced techniques both sensitive to short- and long-range ordering clearly shows the absence of any spatial correlation between Al^{3+} cations from the hydroxide layers and iodide anions from the interlayer, independent of cation charge distribution.

Al^{3+} and Zn^{2+} were found to be distributed at short-range distances in a regular pattern in Zn_2Al-I LDH, generating a honeycomb configuration at long-range distance and a unique hexagonal supercell. A local order of Al^{3+} with an orthorhombic supercell for Zn_3Al LDH was shown here for the first time. This finding was supported by ab initio calculations and FEFF-based wavelet analysis of the EXAFS spectra.

The coordination environment of I^- in the (Mg/Zn)$_r$Al LDH was found by EXAFS spectroscopy to be similar to the one of I^- in water at all M^{2+}/M^{3+} ratios, as indicated by the detection of a single (oxygen) shell at short distance ($R \sim 3.6$ Å) and the large Debye–Waller factors. The absence of backscattering atoms at larger distance indicates a weak coordination between iodide and cations, even if the local distribution of Al^{3+} is ordered. Thus, a large dynamic of interlayer species is possible.

A further consequence of the weak coordination between iodide in the interlayer and cations from the hydroxide layer is a long-range structural disorder, especially stacking faults of the hydroxide sheets (found in the Rietveld refinement and PDF analysis). This results in the lack of correlation between cation and anion position in hydrotalcite-like minerals.

In contrast to the results of this study, preliminary data from an ongoing study show a local order of iodide in hydrocalumite-like minerals (CaAl LDH). In these compounds Ca is 7-fold coordinated to six hydroxides groups and to an interlayer water molecule, resulting in a limited motion of interlayer species and also a reduction of stacking disorder.

ASSOCIATED CONTENT

S **Supporting Information**

(SI.1) Temperature influence on data collection (XRD and EXAFS), (SI.2) comparison of FEFF-calculated paths using different 3D atomic models, (SI.3) I−O radial distribution function from the optimized structure, and (SI.4) Morlet wavelets. This information is available free of charge via the Internet at http://pubs.acs.org.

AUTHOR INFORMATION

Corresponding Author

*E-mail: laure.aimoz@psi.ch. Phone: +41-56-310-5656.

Notes

The authors declare no competing financial interest.

ACKNOWLEDGMENTS

REFERENCES

(1) Johnson, L.; Günther-Leopold, I.; Kobler Waldis, J.; Linder, H. P.; Low, J.; Cui, D.; Ekeroth, E.; Spahiu, K.; Evins, L. S. Rapid aqueous release of fission products from high burn-up LWR fuel: Experimental results and correlations with fission gas release. *J. Nucl. Mater.* **2012**, *420* (1−3), 54−62.

(2) Fernandez, R.; Cuevas, J.; Mäder, U. K. Modeling experimental results of diffusion of alkaline solutions through a compacted bentonite barrier. *Cem. Concr. Res.* **2010**, *40* (8), 1255−1264.

(3) Evans, D. G.; Slade, R. C. T. Structural aspects of layered double hydroxides. In *Layered Double Hydroxides*; Duan, X., Evans, D. G., Ed. Springer-Verlag: Berlin, 2005, 2006; Vol. *119*, pp 1−87.

(4) Drits, V. A.; Bookin, A. S. Crystal structure and X-ray identification of layered double hydroxides. In *Layered Double Hydroxides: Present and Future*; Rives, V., Ed.; Nova Science Publishers Inc.: New York, 2001; 439 pp.

(5) Pauling, L. The principles determining the structure of complex ionic crystals. *J. Am. Chem. Soc.* **1929**, *51*, 1010−1026.

(6) Besserguenev, A. V.; Fogg, A. M.; Francis, R. J.; Price, S. J.; OHare, D.; Isupov, V. P.; Tolochko, B. P. Synthesis and structure of the gibbsite intercalation compounds $[LiAl_2(OH)_6]X$ {X = Cl, Br, NO_3} and $[LiAl_2(OH)_6]Cl·H_2O$ using synchrotron X-ray and neutron powder diffraction. *Chem. Mater.* **1997**, *9* (1), 241−247.

(7) Kuzel, H.-J. Röntgenuntersuchung im System $3CaO·Al_2O_3·CaSO_4·nH_2O−3CaO·Al_2O_3·CaCl_2·nH_2O−H_2O$. *Neues Jahrbuch Mineral. Monatsh.* **1966**, 193−200.

(8) Serna, C. J.; Rendon, J. L.; Iglesias, J. E. Crystal-chemical study of layered $[Al_2Li(OH)_6]^+X^−·nH_2O$. *Clays Clay Miner.* **1982**, *30* (3), 180−184.

(9) Simon, L.; Francois, M.; Refait, P.; Renaudin, G.; Lelaurain, M.; Genin, J. M. R. Structure of the Fe(II-III) layered double hydroxysulphate green rust two from Rietveld analysis. *Solid State Sci.* **2003**, *5* (2), 327−334.

(10) Intissar, M.; Segni, R.; Payen, C.; Besse, J. P.; Leroux, F. Trivalent cation substitution effect into layered double hydroxides $Co_2Fe_yAl_{1−y}(OH)_6Cl·nH_2O$: Study of the local order—Ionic conductivity and magnetic properties. *J. Solid State Chem.* **2002**, *167* (2), 508−516.

(11) Taviot-Guého, C.; Leroux, F.; Payen, C.; Besse, J. P. Cationic ordering and second-staging structures in copper−chromium and zinc−chromium layered double hydroxides. *Appl. Clay Sci.* **2005**, *28* (1−4), 111−120.

(12) Vucelic, M.; Jones, W.; Moggridge, G. D. Cation ordering in synthetic layered double hydroxides. *Clays Clay Miner.* **1997**, *45* (6), 803−813.

(13) Sideris, P. J.; Nielsen, U. G.; Gan, Z. H.; Grey, C. P. Mg/Al ordering in layered double hydroxides revealed by multinuclear NMR spectroscopy. *Science* **2008**, *321* (5885), 113−117.

(14) Cadars, S.; Layrac, G.; Gerardin, C.; Deschamps, M.; Yates, J. R.; Tichit, D.; Massiot, D. Identification and quantification of defects in the cation ordering in Mg/Al layered double hydroxides. *Chem. Mater.* **2011**, *23* (11), 2821−2831.

(15) Yan, H.; Wei, M.; Ma, J.; Evans, D. G.; Duan, X. Plane-wave density functional theory study on the structural and energetic properties of cation-disordered Mg−Al layered double hydroxides. *J. Phys. Chem. A* **2010**, *114* (27), 7369−7376.

(16) Schutz, A.; Biloen, P. Interlamellar chemistry of hydrotalcites. 1. Polymerization of silicate anions. *J. Solid State Chem.* **1987**, *68* (2), 360−368.

(17) Solin, S. A.; Hines, D. R.; Seidler, G. T.; Treacy, M. M. J. Novel structural properties of $Ni_{1−x}Al_x$ layer double hydroxides. *J. Phys. Chem. Solids* **1996**, *57* (6−8), 1043−1048.

(18) Radha, A. V.; Kamath, P. V.; Shivakumara, C. Order and disorder among the layered double hydroxides: Combined Rietveld and DIFFaX approach. *Acta Crystallogr.* **2007**, *B63*, 243−250.

(19) Pisson, J.; Morel, J. P.; Morel-Desrosiers, N.; Taviot-Gueho, C.; Malfreyt, P. Molecular modeling of the structure and dynamics of the interlayer species of ZnAlCl layered double hydroxide. *J. Phys. Chem. B* **2008**, *112* (26), 7856−7864.

(20) Li, H.; Ma, J.; Evans, D. G.; Zhou, T.; Li, F.; Duan, X. Molecular dynamics modeling of the structures and binding energies of alpha-nickel hydroxides and nickel-aluminum layered double hydroxides containing various interlayer guest anions. *Chem. Mater.* **2006**, *18* (18), 4405−4414.

(21) Demel, J.; Kubat, P.; Jirka, I.; Kovar, P.; Pospisil, M.; Lang, K. Inorganic−organic hybrid materials: Layered zinc hydroxide salts with intercalated porphyrin sensitizers. *J. Phys. Chem. C* **2010**, *114* (39), 16321−16328.

(22) Kalinichev, A. G.; Kumar, P. P.; Kirkpatrick, R. J. Molecular dynamics computer simulations of the effects of hydrogen bonding on the properties of layered double hydroxides intercalated with organic acids. *Philos. Mag.* **2010**, *90* (17−18), 2475−2488.

(23) Cygan, R. T.; Greathouse, J. A.; Heinz, H.; Kalinichev, A. G. Molecular models and simulations of layered materials. *J. Mater. Chem.* **2009**, *19* (17), 2470−2481.

(24) Kumar, P. P.; Kalinichev, A. G.; Kirkpatrick, R. J. Molecular dynamics simulation of the energetics and structure of layered double hydroxides intercalated with carboxylic acids. *J. Phys. Chem. C* **2007**, *111* (36), 13517−13523.

(25) Newman, S. P.; Williams, S. J.; Coveney, P. V.; Jones, W. Interlayer arrangement of hydrated MgAl layered double hydroxides containing guest terephthalate anions: Comparison of simulation and measurement. *J. Phys. Chem. B* **1998**, *102* (35), 6710−6719.

(26) Aicken, A. M.; Bell, I. S.; Coveney, P. V.; Jones, W. Simulation of layered double hydroxide intercalates. *Adv. Mater.* **1997**, *9*, (6), 496-&.

(27) Fraccarollo, A.; Cossi, M.; Marchese, L. DFT simulation of Mg/Al hydrotalcite with different intercalated anions: Periodic structure and solvating effects on the iodide/triiodide redox couple. *Chem. Phys. Lett.* **2010**, *494* (4−6), 274−278.

(28) Prasanna, S. V.; Kamath, P. V.; Shivakumara, C. Interlayer structure of iodide intercalated layered double hydroxides (LDHs). *J. Colloid Interface Sci.* **2010**, *344* (2), 508−512.

(29) Prasanna, S. V.; Radha, A. V.; Kamath, P. V.; Kannan, S. Bromide-ion distribution in the interlayer of the layered double hydroxides of Zn and Al: Observation of positional disorder. *Clays Clay Miner.* **2009**, *57* (1), 82−92.

(30) Gomilsek, J. P.; Arcon, I.; de Panfilis, S.; Kodre, A. X-ray absorption in atomic iodine in the K-edge region. *Phys. Rev. A* **2009**, *79* (3), 032514.

(31) Fulton, J. L.; Schenter, G. K.; Baer, M. D.; Mundy, C. J.; Dang, L. X.; Balasubramanian, M. Probing the hydration structure of polarizable halides: A multiedge XAFS and molecular dynamics study of the iodide anion. *J. Phys. Chem. B* **2010**, *114* (40), 12926−12937.

(32) Tanida, H.; Watanabe, I. Dependence of EXAFS (extended X-ray absorption fine structure) parameters of iodide anions in various solvents upon a solvent parameter. *Bull. Chem. Soc. Jpn.* **2000**, *73* (12), 2747−2752.

(33) Yagi, K.; Umezawa, S.; Terauchi, H.; Kasatani, H. EXAFS study of phase transitions in KIO_3. *J. Synchrotron Radiat.* **2001**, *8*, 803−805.

(34) Lezama-Pacheco, J.; de Leon, J. M.; Espinosa, F. J.; Rabago, F.; Conradson, S. Local atomic structure around iodine in ZnSe: I. *Sol. Energy Mater. Sol. Cells* **2004**, *82* (1−2), 151−157.

(35) D'Angelo, P.; Zitolo, A.; Migliorati, V.; Pavel, N. V. Measurement of x-ray multielectron photoexcitations at the I K-edge. *Phys. Rev. B* **2008**, *78* (14), 144105.

(36) Michel, T.; Alvarez, L.; Sauvajol, J. L.; Almairac, R.; Aznar, R.; Bantignies, J. L.; Mathon, O. EXAFS investigations of iodine-doped carbon nanotubes. *Phys. Rev. B* **2006**, *73* (19), 195419.

(37) Feiters, M. C.; Kupper, F. C.; Meyer-Klaucke, W. X-ray absorption spectroscopic studies on model compounds for biological iodine and bromine. *J. Synchrotron Radiat.* **2005**, *12*, 85−93.

(38) Neilson, J. R.; Kurzman, J. A.; Seshadri, R.; Morse, D. E. Cobalt coordination and clustering in α-$Co(OH)_2$ revealed by synchrotron X-ray total scattering. *Chem. Eur. J.* **2010**, *16* (33), 9998−10006.

(39) Miyata, S. Anion-exchange properties of hydrotalcite-like compounds. *Clays Clay Miner.* **1983**, *31* (4), 305−311.

(40) Kameda, T.; Yoshioka, T.; Watanabe, K.; Uchida, M.; Okuwaki, A. Dehydrochlorination behavior of a chloride ion-intercalated hydrotalcite-like compound during thermal decomposition. *Appl. Clay Sci.* **2007**, *35* (3−4), 173−179.

(41) Lv, L. A.; He, J.; Wei, M.; Evans, D. G.; Duan, X. Uptake of chloride ion from aqueous solution by calcined layered double hydroxides: Equilibrium and kinetic studies. *Water Res.* **2006**, *40* (4), 735−743.

(42) Rodriguez-Carvajal, J. Recent advances in magnetic-structure determination by neutron powder diffraction. *Physica B* **1993**, *192* (1−2), 55−69.

(43) Roisnel, T.; Rodriguez-Carvajal, J. WinPLOTR: A Windows tool for powder diffraction patterns analysis. *Proceedings of the Seventh European Powder Diffraction Conference (EPDIC 7), 2000*; Dehlez, R., Moittenmeijer, E. J., Eds.; Material Science Forum: 2000; pp 118−123.

(44) Thompson, P.; Cox, D. E.; Hastings, J. B. Rietveld refinement of Debye−Scherrer synchrotron X-ray data from Al_2O_3. *J. Appl. Crystallogr.* **1987**, *20*, 79−83.

(45) Jarvinen, M. Application of symmetrized harmonics expansion to correction of the preferred orientation effect. *J. Appl. Crystallogr.* **1993**, *26*, 525−531.

(46) Langford, J. I.; Louer, D. Diffraction line-profiles and Scherrer constants for materials with cylindrical crystallites. *J. Appl. Crystallogr.* **1982**, *15* (Feb), 20−26.

(47) Stephens, P. W. Phenomenological model of anisotropic peak broadening in powder diffraction. *J. Appl. Crystallogr.* **1999**, *32*, 281−289.

(48) Billinge, S. J. L. Nanoscale structural order from the atomic pair distribution function (PDF): There's plenty of room in the middle. *J. Solid State Chem.* **2008**, *181* (7), 1695−1700.

(49) Qiu, X.; Thompson, J. W.; Billinge, S. J. L. PDFgetX2: A GUI-driven program to obtain the pair distribution function from X-ray powder diffraction data. *J. Appl. Crystallogr.* **2004**, *37*, 678.

(50) Proffen, T.; Billinge, S. J. L. PDFFIT, a program for full profile structural refinement of the atomic pair distribution function. *J. Appl. Crystallogr.* **1999**, *32*, 572−575.

(51) Renaudin, G.; Rapin, J. P.; Elkaim, E.; Francois, M. Polytypes and polymorphs in the related Friedel's salt $[Ca_2Al-(OH)_6]^+[X \cdot 2H_2O]^-$ halide series. *Cem. Concr. Res.* **2004**, *34* (10), 1845−1852.

(52) van Beek, W.; Safonova, O. V.; Wiker, G.; Emerich, H. SNBL, a dedicated beamline for combined in situ X-ray diffraction, X-ray absorption and Raman scattering experiments. *Phase Transitions* **2011**, *84* (8), 726−732.

(53) Hohenberg, P.; Kohn, W. Inhomogeneous electron gas. *Phys. Rev. B* **1964**, *136*, (3B), B864-&.

(54) VandeVondele, J.; Krack, M.; Mohamed, F.; Parrinello, M.; Chassaing, T.; Hutter, J. QUICKSTEP: Fast and accurate density functional calculations using a mixed Gaussian and plane waves approach. *Comput. Phys. Commun.* **2005**, *167* (2), 103−128.

(55) Goedecker, S.; Teter, M.; Hutter, J. Separable dual-space Gaussian pseudopotentials. *Phys. Rev. B* **1996**, *54* (3), 1703−1710.

(56) VandeVondele, J.; Hutter, J., Gaussian basis sets for accurate calculations on molecular systems in gas and condensed phases. *J. Chem. Phys.* **2007**, *127*, (11).

(57) Perdew, J. P.; Burke, K.; Ernzerhof, M. Generalized gradient approximation made simple. *Phys. Rev. Lett.* **1996**, *77* (18), 3865−3868.

(58) Grimme, S. Semiempirical GGA-type density functional constructed with a long-range dispersion correction. *J. Comput. Chem.* **2006**, *27* (15), 1787−1799.

(59) Baer, M. D.; Pham, V.-T.; Fulton, J. L.; Schenter, G. K.; Balasubramanian, M.; Mundy, C. J. Is iodate a strongly hydrated cation? *J. Phys. Chem. Lett.* **2011**, *2* (20), 2650−2654.

(60) Borsboom, M.; Bras, W.; Cerjak, I.; Detollenaere, D.; van Loon, D. G.; Goedtkindt, P.; Konijnenburg, M.; Lassing, P.; Levine, Y. K.; Munneke, B.; Oversluizen, M.; van Tol, R.; Vlieg, E. The Dutch-Belgian beamline at the ESRF. *Journal of Synchrotron Radiation* **1998**, *5*, 518−520.

(61) Newville, M. IFEFFIT: Interactive XAFS analysis and FEFF fitting. *J. Synchrotron Radiat.* **2001**, *8*, 322−324.

(62) Ravel, B.; Newville, M. ATHENA, ARTEMIS, HEPHAESTUS: Data analysis for X-ray absorption spectroscopy using IFEFFIT. *J. Synchrotron Radiat.* **2005**, *12*, 537−541.

(63) Manceau, A.; Chateigner, D.; Gates, W. P. Polarized EXAFS, distance-valence least-squares modeling (DVLS), and quantitative texture analysis approaches to the structural refinement of Garfield nontronite. *Phys. Chem. Miner.* **1998**, *25* (5), 347−365.

(64) O'day, P. A.; Rehr, J. J.; Zabinsky, S. I.; Brown, G. E. Extended X-ray-absorption fine-structure (EXAFS) analysis of disorder and multiple-scattering in complex crystalline solids. *J. Am. Chem. Soc.* **1994**, *116* (7), 2938−2949.

(65) Ankudinov, A. L.; Rehr, J. J. Theory of solid-state contributions to the X-ray elastic scattering amplitude. *Phys. Rev. B* **2000**, *62* (4), 2437−2445.

(66) Rehr, J. J.; Deleon, J. M.; Zabinsky, S. I.; Albers, R. C. Theoretical X-ray absorption fine-structure standards. *J. Am. Chem. Soc.* **1991**, *113* (14), 5135−5140.

(67) Funke, H.; Chukalina, M.; Scheinost, A. C. A new FEFF-based wavelet for EXAFS data analysis. *J. Synchrotron Radiat.* **2007**, *14*, 426−432.

(68) Shannon, R. D. Revised effective ionic-radii and systematic studies of interatomic distances in halides and chalcogenides. *Acta Crystallogr.* **1976**, *A32* (Sep1), 751−767.

(69) Bellotto, M.; Rebours, B.; Clause, O.; Lynch, J.; Bazin, D.; Elkaim, E. A reexamination of hydrotalcite crystal chemistry. *J. Phys. Chem.* **1996**, *100* (20), 8527−8534.

(70) Vespa, M.; Dahn, R.; Grolimund, D.; Wieland, E.; Scheidegger, A. M. Spectroscopic investigation of Ni speciation in hardened cement paste. *Environ. Sci. Technol.* **2006**, *40* (7), 2275−2282.

(71) Jacquat, O.; Voegelin, A.; Villard, A.; Marcus, M. A.; Kretzschmar, R. Formation of Zn-rich phyllosilicate, Zn-layered double hydroxide and hydrozincite in contaminated calcareous soils. *Geochim. Cosmochim. Acta* **2008**, *72* (20), 5037−5054.

(72) Scheinost, A. C.; Sparks, D. L. Formation of layered single- and double-metal hydroxide precipitates at the mineral/water interface: A multiple-scattering XAFS analysis. *J. Colloid Interface Sci.* **2000**, *223* (2), 167−178.

(73) Voegelin, A.; Kretzschmar, R. Formation and dissolution of single and mixed Zn and Ni precipitates in soil: Evidence from column experiments and extended X-ray absorption fine structure spectroscopy. *Environ. Sci. Technol.* **2005**, *39* (14), 5311−5318.

(74) Hines, D. R.; Solin, S. A.; Costantino, U.; Nocchetti, M. Unique composition-dependent basal expansion of CO_3−Cl (H_2O) layer double hydroxides. *Solid State Commun.* **1998**, *108* (12), 971−976.

(75) Hofmeister, W.; von Platen, H. Crystal chemistry and atomic order in brucite-related double-layer structures. *Crystallogr. Rev.* **1992**, *3* (1), 3−26.